

Confined fluid and the fluid-solid transition: Evidence from absolute free energy calculationsLi Wan,¹ Christopher R. Iacovella,¹ Trung D. Nguyen,² Hugh Docherty,¹ and Peter T. Cummings^{1,3}¹*Department of Chemical and Biomolecular Engineering, Vanderbilt University, Nashville, Tennessee, 37235-1604, USA*²*Oak Ridge National Laboratory, Oak Ridge, Tennessee 37831-6494, USA*³*Center for Nanophase Materials Sciences, Oak Ridge National Laboratory, Oak Ridge, Tennessee 37831-6494, USA*

(Received 27 September 2012; revised manuscript received 24 November 2012; published 11 December 2012)

The debate on whether an organic fluid nanoconfined by mica sheets will undergo a fluid-to-solid transition as the fluid film thickness is reduced below a critical value has lasted over two decades. Extensive experimental and simulation investigations have thus far left this question only partially addressed. In this work, we adapt and apply absolute free energy calculations to analyze the phase behavior of a simple model for nanoconfined fluids, consisting of spherical Lennard-Jones (LJ) molecules confined between LJ solid walls, which we use in combination with grand-canonical molecular dynamics simulations. Absolute Helmholtz free energy calculations of the simulated nanoconfined systems directly support the existence of order-disorder phase transition as a function of decreasing wall separation, providing results in close agreement with previous experiments and detailed atomistic simulations.

DOI: [10.1103/PhysRevB.86.214105](https://doi.org/10.1103/PhysRevB.86.214105)

PACS number(s): 64.60.Cn, 64.70.Nd

I. INTRODUCTION

Nanoconfined fluids are important in a wide range of applications, including adsorption in industrial processes and the lubrication of computer hard drives and artificial joints.¹⁻³ Since the early 1990s, there has been a debate over whether an organic fluid transitions from a disordered, liquid state to an ordered solid phase as the separation between the two confining surfaces, composed of molecularly smooth mica, drops below a critical value, typically six or seven molecular diameters. Following the initial observation of nanoconfinement-induced solidification by Israelachvili and co-workers using surface force apparatus (SFA),⁴ surface force balance (SFB) experiments by Klein and co-workers⁵⁻⁷ on octamethylcyclotetrasiloxane (OMCTS) nanoconfined between two atomically smooth mica surfaces suggest a first-order phase change when the pore separation is reduced from seven to six molecular layers. In their experiments, they observe a nonzero yield stress characteristic of a solid, along with a several-orders-of-magnitude increase in viscosity. However, experiments by Granick and co-workers⁸ using SFA instead suggest a second-order transition; for sufficiently slow rates of confinement, they did not observe a dramatic viscosity increase or evidence of a nonzero yield stress. Currently, no agreement has been reached between these two results, in large part due to the intrinsic difficulties faced in experiment.⁹ Specifically, the confined phase is buried between two solid mica walls with just a few layers of material contained in this region, which has thus far made it impossible to directly observe the structure. Moreover, the discovery of platinum nanoparticles on the mica surfaces in some experiments^{10,11} led to a reexamination of previously published results, with the conclusion that some experimental findings were potentially compromised.¹² More recent experiments have provided additional insights into this debate; several studies have found results consistent with the work of Klein and Kumacheva,¹³⁻¹⁵ while others have shown agreement with the conclusions of Granick.^{16,17} Atomic force microscopy (AFM), with a much smaller contact area than SFB and SFA, has also been applied to study the confinement of organic fluids.¹⁸⁻²⁰ These AFM studies found that the

viscosity of a confined organic fluid stays bulklike down to three molecular layers before exhibiting enhancements in the viscosity as the last two fluid layers are expelled;²⁰ these results are similar to the work of Granick and co-workers, although it is important to note that pyrolytic graphite confining surfaces were used rather than mica. However, Mugele and co-workers²¹ have raised questions about the suitability of AFM for the study of confinement-induced solidification. Specifically, due to the nonmonotonic nature of nanoconfined fluid properties, they found that the typically assumed relation between molecular diffusivity and the damping measured by the AFM tip does not hold for nanoconfined fluids. Over the last two decades, despite significant advances in experimental methods,²² there remains no general agreement among major experimental groups with respect to the existence of a sharp order-disorder transition as a function of surface separation.

The ability of molecular simulation to resolve the spatial coordinates of confined particles and eliminate nonidealities has made it a valuable tool in this debate. Pioneering work, starting in the early 1990s, revealed confinement-induced extra ordering in idealized systems.²³ More comprehensive investigations, focusing on nanoconfinement-induced solidification, were initiated in the late 1990s,^{24,25} employing models and conditions much closer to experimental scenarios. These results further support the case of nanoconfinement-induced solidification and reveal dynamics and structural shifts due to confinement. Seminal work by Radhakrishnan and Gubbins^{26,27} examined the behavior of a model system composed of Lennard-Jones spheres under smooth wall confinement, providing strong evidence of the existence of a first-order phase transition. In particular, their studies employed umbrella sampling to calculate the relative free energy difference between a confined disordered phase and a confined solid phase, demonstrating that the solid phase was lower in free energy over a wide range of state points. They additionally demonstrated that the order-disorder transition temperature shifts to higher values as the wall-fluid interaction exceeds the fluid-fluid interaction. However, Jabbarzadeh and co-workers^{28,29} argued that a metastable high-friction fluid film

forms rather than a thermodynamically stable solid, supporting the argument that the transition is second order.

Simulation is not without its own challenges. Most simulation studies, including the aforementioned work, have made use of simplified models, which may neglect important characteristics of the experimental systems. The rigor of these studies has grown with increasing computational power, such as the recent simulations by Cummings and co-workers^{3,30} where fully atomistic models of both the mica surfaces and confined molecules were used. This recent work demonstrated the formation of ordered structures at fewer than six layers of fluid, in close agreement with prior work using simplified models.³¹ The surprising conclusion of these atomistically detailed simulations^{3,30} is that the order-disorder transition in nonpolar linear and cyclic alkanes nanoconfined between mica sheets is driven by electrostatic interactions between the confined fluid and the mica surfaces. Similar atomistically detailed simulations of water, a polar solvent, nanoconfined between mica surfaces further emphasize this, showing that water does not undergo an order-disorder phase transition until a separation of one to two water layers,^{32,33} in agreement with experimental results.^{34,35} However, despite advances in model detail and computational resources, the accessible length and time scales in simulation are still considerably limited compared to experiment. This makes it possible that the observed order-disorder transitions seen in simulations are not thermodynamically stable over a sufficiently long time or in sufficiently large systems.

In this work, we employ a combined approach to examine the behavior of Lennard-Jones (LJ) spheres under nanoconfinement, using both grand-canonical molecular dynamics simulations³⁶ and absolute free energy calculations.^{37,38} Calculations of the free energy are carried out using the Einstein crystal method,^{37,38} originally proposed for bulk solids, which we adapt for nanoconfined systems. The absolute free energy calculations provide a more conclusive determination of the stability of the simulation results, providing additional insight regarding the structure and transitions that occur as a result of nanoconfinement. In particular, our work focuses on analysis of the behavior of the “central layers,” i.e., those not in contact with the pore walls, highlighting their importance in determining phase transitions.

II. MODEL AND METHODS

We use a simple, generic model of a nanoconfined system, composed of identically sized Lennard-Jones spherical particles (i.e., $\sigma = 1$), where all parameters are given in reduced LJ units based on the mobile fluid particle parameters ($T^* = k_B T / \epsilon_{mm}$, $\rho^* = \rho \sigma^3$). Systems are composed of two particle species: mobile fluid particles and static wall particles. The interaction between mobile fluid particles is fixed at $\epsilon_{mm} = 1.0$ for all simulations, whereas the interaction between the walls and mobile particles is varied, e.g., $\epsilon_{wm} = (1.0, 2.0, 4.0)$. The upper end of these values provides a reasonable approximation of the interaction between mica and organic molecules; previous work has parametrized the interaction strength of mica-CH₂ at $\epsilon_{wm} \sim 4.47\epsilon_{mm}$.²⁵ Walls are constructed of spheres in a minimum potential energy fcc structure, corresponding to number density $\rho^* = 1.0$. Walls

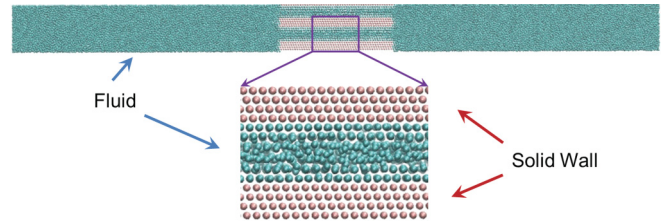


FIG. 1. (Color online) Snapshot of a typical GCMD simulation. In this case, two pores constructed of stationary particles are embedded within a large bulk fluid, with periodic boundary conditions in all dimensions

are oriented such that the “ABC” stacking planes are parallel to the pore interface (i.e., z , the [111] fcc direction, is normal to the pore wall).

A. GCMD simulations

We perform grand-canonical molecular dynamics (GCMD) simulations as pioneered by Gao and Landman.³⁶ Our GCMD simulations consist of a fcc slit nanopore embedded within a large, rectilinear bulk system, allowing for the free exchange of particles between the pore and the bulk environment (see Fig. 1). In the system, most of the total particles exist in the bulk state with $\rho^* = 0.85$. As a result, particles in the bulk are essentially unaffected by changes within the pore. Here, we perform simulations at constant number of particles N , volume V , and temperature T (i.e., NVT); while GCMD simulations are often performed at constant pressure P (i.e., NPT), the large size of the bulk fluid makes the use of NPT unnecessary, as we see negligible changes in system pressure as a function of time. Here, we perform two different sets of simulations. The first set of simulations consists of GCMD simulations of 86 000 total particles and are used to investigate the order-disorder transition and as input to the free energy calculations. These are performed with both the HOOMD-BLUE (Refs. 39 and 40) and LAMMPS (Ref. 41) simulation packages using the Nose-Hoover thermostat with time step = 0.001 in LJ units; HOOMD-BLUE is used for calculations performed on clusters equipped with graphical processing units (GPU), whereas LAMMPS is used for parallel simulations on traditional distributed CPU systems. Both packages produced indistinguishable results. Simulations use the XPLOR style shifting, leaving the well depth unchanged as a result of potential truncation and shifting. The cutoff of the interaction between mobile particles is set to 3σ , where XPLOR shifting starts at 2.75σ . The wall-mobile particle interaction cutoff is set to 5.0σ , with XPLOR shifting starting at 4.75σ . Since the wall-mobile particle interaction energy will, in general, exceed the interaction between mobile particles, a larger cutoff is required to minimize artifacts associated with truncation. This longer cutoff and XPLOR shifting is also used to ensure better continuity with free energy calculations. The second set of simulations consists of large-scale GCMD simulations with 960 000 and 6 220 000 total particles used to investigate the effects of surface contact area on ordering. These simulations are carried out using a hybrid GPU-CPU version of LAMMPS,⁴¹ capable of efficiently scaling to millions of particles. These simulations also use the Nose-Hoover thermostat with time step 0.005 and XPLOR shifting.

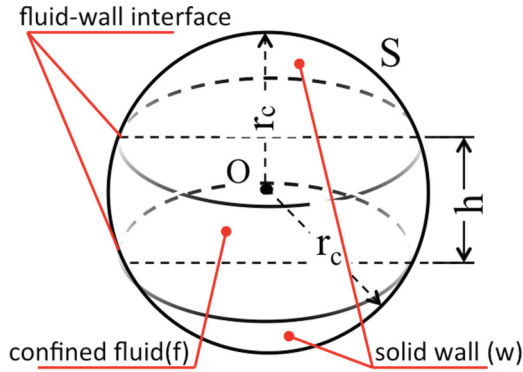


FIG. 2. (Color online) Schematic representation of modified tail correction.

B. Free energy calculations

Absolute Helmholtz free energy (A) calculations for confined solid states are performed using the Einstein crystal method originally introduced by Frenkel and Ladd³⁷ and revisited in detail by Vega and co-workers.^{42,43} This method allows us to compute the free energy of a given solid structure by creating an integration path linking it to an Einstein crystal with the same structure. The Einstein crystal method was originally proposed for the calculation of bulk solid crystals and, therefore, modifications are required to properly adapt this free energy method to nanoconfined systems. Even though our model system is composed of identically sized LJ spheres, the strongly differing interaction strengths make the system heterogeneous. As such, using a standard tail correction in the nanoconfined system would result in systematic errors, making it difficult to explicitly compare with, e.g., bulk phases or different pore heights. To account for this, a modified tail correction is proposed (shown graphically in Fig. 2):

$$\begin{aligned}
 U^{\text{tail}} &= \frac{1}{2} \int_{r_c}^{\infty} dr \rho S U(r) \\
 &= \frac{1}{2} \int_{r_c}^{\infty} dr [\rho_m S_m U_{mm}(r) + \rho_w S_w U_{wm}(r)] \\
 &= 2\pi h \rho_m \epsilon_{mm} \sigma_{mm}^2 \left\{ \frac{1}{5} \left(\frac{\sigma_{mm}}{r_c} \right)^{10} - \frac{1}{2} \left(\frac{\sigma_{mm}}{r_c} \right)^4 \right\} \\
 &\quad - 2\pi h \rho_w \epsilon_{wm} \sigma_{wm}^2 \left\{ \frac{1}{5} \left(\frac{\sigma_{wm}}{r_c} \right)^{10} - \frac{1}{2} \left(\frac{\sigma_{wm}}{r_c} \right)^4 \right\} \\
 &\quad + \frac{8}{3} \pi \rho_w \epsilon_{wm} \sigma_{wm}^3 \left\{ \frac{1}{3} \left(\frac{\sigma_{wm}}{r_c} \right)^9 - \left(\frac{\sigma_{wm}}{r_c} \right)^3 \right\},
 \end{aligned}$$

where S is the surface area of spherical shell (including the surface area of the partial sphere in nanoconfined phase and that in solid wall), r_c is the cutoff distance used in potential calculation, h is the separation, and the subscripts m and w represent mobile fluid particles and static wall particles, respectively. A detailed step-by-step derivation and validation is included in the Supplemental Material.⁴⁴ The requirement for this formula is that the cutoff distance should be equal to or larger than the separation of the pore. For simplicity, we assume that particles in the solid walls are static; this is reasonable given the fact that strongly interacting crystalline

wall particles will be much more tightly bound to their lattice positions than mobile fluid particles. This assumption has been used in prior work by Dominguez and co-workers⁴⁵ who also used the Einstein crystal method to calculate the free energy of nanoconfined phases, however, they focused on systems with weak wall-mobile particle interactions (i.e., $\epsilon_{wm} < \epsilon_{mm}$) and did not make use of our modified tail correction to avoid systematic errors. Additionally, while we use Monte Carlo (MC) simulations in the first stage to calculate the free energy difference between a system of interacting particles and noninteracting particles both attached to lattice points, we use Nose-Hoover MD simulations within LAMMPS (Ref. 41) to sample the various state points in the second stage (i.e., removing the harmonic potential), rather than a more standard MC-based approach. MD allows for the efficient use of multiple CPUs reducing the computation time for this calculation. We find that the use of MD has a negligible impact on the accuracy of the method, e.g., $A = 2.618 N k_B T$ versus $2.601 N k_B T$,⁴² as calculated via MD and MC, respectively, for a bulk fcc LJ solid at $\rho^* = 1.28$ and $T^* = 2.0$ (note, N is number of particles, k_B is Boltzmann constant, and T is temperature).

III. RESULTS AND DISCUSSION

A. Ideal systems

We begin by revisiting the impact of the wall-mobile fluid interaction strength on the order-disorder transition (ODT) of nanoconfined fluids. This allows us to establish boundaries for the specific model and parameters we use here, as well as to test the adapted free energy method. Previous simulation work predicts that as the interaction strength between walls and mobile fluid particles (ϵ_{wm}) is increased to values exceeding the fluid-fluid interaction (ϵ_{mm}), the order-disorder transition (ODT) will shift to higher temperatures than an equivalent bulk system.^{27,31} To examine this, we perform GCMD simulations starting from a high-temperature disordered state at $T^* = 4.0$, cooling by increments of $\Delta T^* = 0.1$ until a low-temperature solid is achieved. The ODT is estimated via visual inspection and examination of a layer-by-layer global two-dimensional (2D) hexagonal order parameter (OP) of particles within the pore, constructed by taking the Fourier transform with frequency $\ell = 6$ of the superposition of the in-plane first-neighbor shell surrounding atoms within a given layer;^{46,47} a perfectly ordered layer will result in an OP value of unity. For reference, $T_{\text{ODT}}^{\text{bulk}} \sim 0.9$ for a bulk system at $\rho^* = 1$ (note, $\rho^* = 1$ is the density of an ideal minimal potential energy fcc crystal). Table I summarizes the ODT for ideal pore separations [i.e., integer multiples of the fcc layer spacing $2^{(1/6)} \sqrt{(6/9)} \sigma$],

TABLE I. T_{ODT} estimated using GCMD simulations with resolution $\Delta T^* = 0.1$.

No. layers	Separation (σ)	$T_{\text{ODT}}^{\text{conf}} (\epsilon_{wm} = 1)$	$T_{\text{ODT}}^{\text{conf}} (\epsilon_{wm} = 2)$	$T_{\text{ODT}}^{\text{conf}} (\epsilon_{wm} = 4)$
3	2.75	1.7	2.3	3.0
4	3.67	1.4	1.8	2.3
5	4.58	1.1	1.4	1.7
6	5.50	0.9	1.1	1.2
7	6.42	0.8	0.9	1.0

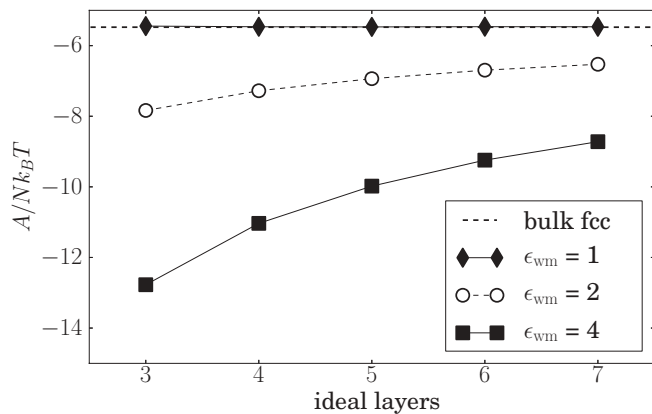


FIG. 3. Absolute Helmholtz free energy ($A/Nk_B T$) as a function of pore size at $T^* = 0.75$ of ideal confined fcc crystal at $\rho^* = 1.0$. $A/Nk_B T$ of the bulk LJ fcc crystal is given by von der Hoefs equation (Ref. 49).

for various ϵ_{wm} values. We observe that as ϵ_{wm} is increased, so too does T_{ODT}^{conf} , in agreement with previous work.^{27,48} The ODT is also shifted to higher temperatures as the pore separation is reduced. This is likely a consequence of the fact that larger pores have a smaller fraction of the total number of confined particles in contact with the walls. Also, we observe that even when interactions are symmetric ($\epsilon_{wm} = \epsilon_{mm} = 1$), small pores demonstrate a slight increase in T_{ODT}^{conf} as compared to the bulk phase. We note that as we exceed six ideal layers, $T_{ODT}^{conf} \sim T_{ODT}^{bulk}$, within the accuracy of our ODT calculations and density variations within the pore.

To unambiguously assess the trends predicted by the GCMD simulations, we employ the modified Einstein crystal method to calculate the absolute Helmholtz free energy for idealized confined fcc systems. In Fig. 3, we plot $A/Nk_B T$ of ideal confined fcc structures as a function of separation, for various ϵ_{wm} values. These calculations are performed at $T^* = 0.75$ as it is below the bulk ODT, and thus all separations should exhibit a stable solid structure. Not surprisingly, $A/Nk_B T$ is reduced as ϵ_{wm} is increased; reducing $A/Nk_B T$ means the phase is more stable relative to the bulk, which manifests itself in $T_{ODT}^{conf} > T_{ODT}^{bulk}$. We also observe that $A/Nk_B T$ is lower for smaller pores than larger pores, and thus smaller pores should likewise be expected to have a higher ODT value than the bulk. These results are fully consistent with previous studies by Gubbins and co-workers²⁷ and Kaneko and co-workers.⁴⁸

B. Nonideal configurations

Focusing our attention on the $\epsilon_{wm} = 4$ system, as this strength is roughly characteristic of mica-organic molecule interactions, we perform GCMD simulations as a continuous function of separation, not just ideal pore spacings. Each pore separation is an independent simulation employing stationary walls and thus we do not need to consider the effects of pore compression rate.^{3,50} In Fig. 4(a), we plot the number density ρ^* of the confined region as a function of separation for systems at $T^* = 1.0$; simulations are generated by slowly cooling from a high-temperature disordered state. At $T^* = 1.0$, solid structures form within the nanopores over the entire range sampled in Fig. 4, while the bulk region of the GCMD

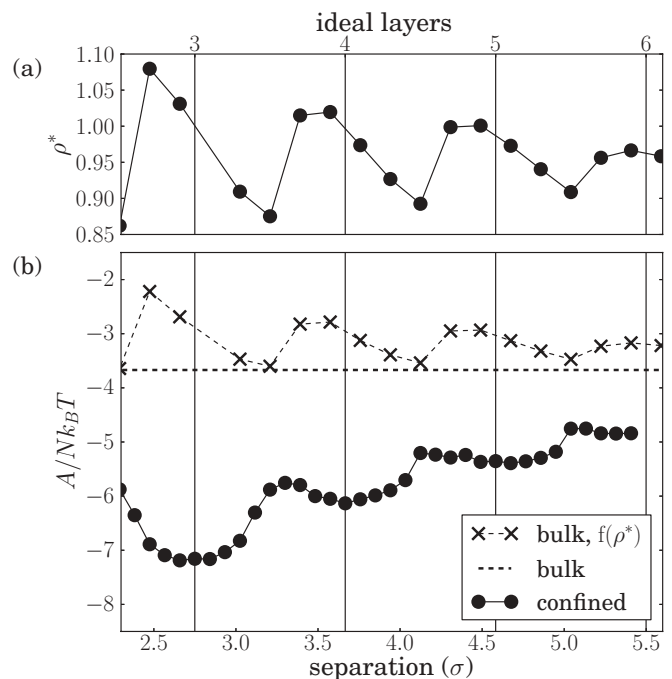


FIG. 4. (a) Number density of particles in the pore as a function of separation, calculated via GCMD simulation. (b) $A/Nk_B T$ of the nanoconfined solid structure as a function of separation, using structures generated via GCMD simulation in part (a) as input. Also plotted is $A/Nk_B T$ of the bulk fluid at $\rho^* = 0.85$, corresponding to the density of the bulk phase in the GCMD simulation. $A/Nk_B T$ of a bulk liquid (calculated at the ρ^* of the confined region) as a function of the nanopore separation is also plotted. Both plots share the same scale on the x axis, with the true separation at bottom, and the separations that correspond to ideal layers at top and as solid vertical lines.

simulation remains in a disordered fluid state. In Fig. 4(a), we observe oscillations in the density of fluid in the pore, where peaks occur just prior to the transition between integer number of layers. Ideal separations occur roughly midway between the peak on the left and valley on the right, with $\rho^* \sim 1$ (i.e., the density of the energetic minimum fcc crystal). The height of this transition peak increases as pore separation is reduced.

Using the configurations generated via simulation as input, we use the modified Einstein crystal method to calculate $A/Nk_B T$ as a function of separation, as plotted in Fig. 4(b). We observe clear peaks and valleys in the free energy curve, where the valley minimums correspond to ideal separations (i.e., perfect spacing for fcc) and peaks occur at the transitions between integer number of layers. For ideal separations, $A/Nk_B T$ of the nanoconfined solid is significantly lowered as separation is reduced, as was seen in Fig. 3. The difference in the peak height *versus* valley depth of the free energy curve is most significant for small separations, whereas the differences are relatively minor for larger separations. That is, there is a smaller penalty for transitioning between integer layer numbers as the pore size is increased. Also plotted in Fig. 4(b) is the free energy of the bulk region of the GCMD simulation at $\rho^* = 0.85$, as calculated using the Johnson equation.⁵¹ We see that, over the entire range, $A/Nk_B T$ of the nanoconfined region is lower than the bulk phase it is in contact with. As

such, there is a strong thermodynamic driving force associated with forming a solid phase within the pore. For additional comparison, we use the density within the pore as input to the Johnson equation, i.e., we compare to the free energy of a disordered liquid at the same density as the solid within the pore. $A/Nk_B T$ of a liquid state scales with density,⁵¹ whereas the solid phase demonstrates a more complex density behavior related to the ability to accommodate the crystal structure.

C. The role of the central atoms

Our results thus far have only considered comparisons between bulk phases and nanoconfined solids. The free energy of a nanoconfined disordered liquid may actually be lower than the equivalent bulk phase, based on the contribution of the wall-fluid potential energy (U) to the total free energy ($A = U - TS$). Thus, while we have clearly shown that nanoconfined solids have lower free energy than equivalent bulk phases, we have not shown via direct absolute free energy calculations that nanoconfined solids have lower free energy than nanoconfined disordered liquids. Calculating the absolute free energy of a nanoconfined fluid directly is challenging, as the simulated systems appear to be strongly driven towards forming ordered solid structures, unless an external bias is applied. Recall that previous work²⁷ employed umbrella sampling to investigate the relative free energy difference between nanoconfined solids and nanoconfined disordered fluids (note, umbrella sampling includes a biasing criteria allowing sampling of regions of phase space that would otherwise be unlikely to be visited during a typical simulation).

Rather than employing a biasing scheme, we can take advantage of the heterogeneous nature of nanoconfined systems to provide further insight into the phase transition. Specifically, it has been previously observed that particles that occupy the central most region of the nanopore strongly dictate the ODT.²⁷ A recent study of confined hard-sphere fluids reveals that the position of particles perpendicular to the solid wall determines their diffusive dynamics, where particles near the wall move much more slowly even in the absence of a strong wall-fluid interaction.⁵² Particles in the central region, those not in contact with the wall, experience the weakest levels of wall-mobile fluid interaction and highest mobility, tending to lag behind regions closer to the walls in terms of structural ordering. The entire system can not be considered a solid until this central region transitions from disordered to ordered. In Fig. 5, we plot the 2D global hexagonal OP as a function of T^* for different spatial regions in the pore, for a system that can accommodate six ideal layers. Particles along the pore walls demonstrate a high value of the OP, even at high T^* , slowly increasing as T^* is reduced. Structural ordering of the particles in the central most layer lag significantly behind the wall region and demonstrate a more rapid transition to an ordered state as T^* is reduced. The spatially intermediate second layer from the wall has characteristics more closely matching the central most layer as opposed to the layer in contact with the wall.

Following this, we make the assumption that, due to the significantly increased ordering at high T^* , particles along the walls effectively act as the confining surface for the central region as it orders, allowing us to treat the layers in contact with the walls as stationary within the free energy calculation.

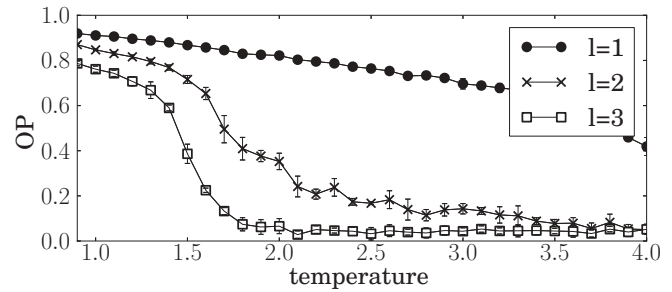


FIG. 5. Global version of the 2D hexagonal order parameter as a function of location within a six-layer pore for $\epsilon_{wm} = 4.00$. $l = 1$ corresponds to the layer in contact with the wall, $l = 3$ corresponds to the third layer, farthest from either wall.

Again, since these central layers dominate in determining when and if the system undergoes an ODT, comparing the free energy of this region to the bulk state is more appropriate as it mostly eliminates the contribution of the strong wall-mobile fluid potential energy to the total free energy.

In Fig. 6(a), we plot $A/Nk_B T$ of the central region of the nanoconfined system with $\epsilon_{wm} = 4.0$, simulated at $T^* = 1.0$; we also plot $A/Nk_B T$ of the full nanoconfined system [identical to Fig. 4(b)] and $A/Nk_B T$ of the bulk disordered fluid at the same density as the pore, calculated using the Johnson equation. The free energy of the central region still demonstrates fluctuations in $A/Nk_B T$, where peaks occur for nonideal separations and valleys for ideal separations. Interestingly, $A/Nk_B T$ of the central most confined region and the equivalent density bulk fluid appear to oscillate with respect to each other; the fluid state is lower in free energy for nonideal separations, whereas the confined solid is lower for

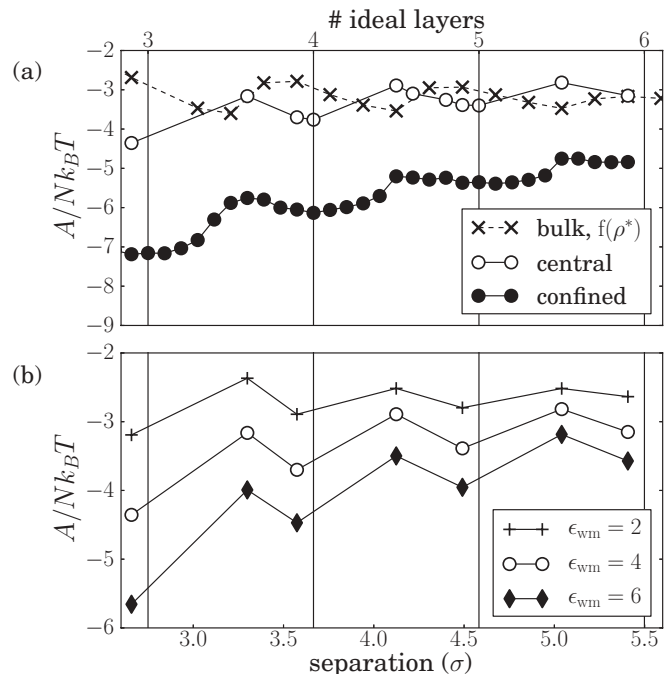


FIG. 6. (a) $A/Nk_B T$ of the central region of the pore (i.e., excluding particles along the walls) as compared to the entire confined region and the bulk value at matching density. (b) $A/Nk_B T$ as function of the central region for $\epsilon_{wm} = [2,4,6]$.

ideal separations. This agrees with calculations by Kaneko and co-workers that suggest the freezing/melting points oscillate with separation.⁴⁸ This trend persists up to approximately six ideal layers, at which point the values of $A/Nk_B T$ converge. This strongly suggests that for larger separations there is no longer a sufficient driving force for crystallization in the central region of the pore, consistent with the previous ODT calculations in Table I, where we saw that $T_{\text{ODT}}^{\text{conf}} \sim T_{\text{ODT}}^{\text{bulk}}$ for greater than six layers when $\epsilon_{\text{wm}} = 4.0$. The fact that the solid state is not universally lower in free energy may help to explain why evidence of a fluid-solid transition is not observed in all experiments, e.g., if the system is compressed to a nonideal spacing for the fluid.

It is important to note that while this comparison largely factors out the strong wall-fluid interaction, the free energy of the equivalent bulk state does not take into account the effects of confinement on the entropy. Confinement will reduce entropy,⁵³ resulting in an increase in total free energy, as compared to a bulk state, and the free energy should increase as pore size is reduced.

In Fig. 6(b), we compare $A/Nk_B T$ of the central region for various values of ϵ_{wm} . As ϵ_{wm} is reduced to 2, $A/Nk_B T$ is shifted upwards, resulting in convergence with the free energy of an equivalent density bulk phase at a smaller separation (~ 5 layers). Similarly, increasing ϵ_{wm} to 6, $A/Nk_B T$ of the central region is lowered, shifting convergence with the equivalent density bulk system to a separation exceeding six layers. This is consistent with the trends in ODT in Table I, where systems with low values of ϵ_{wm} transitioned to bulklike ODT values at smaller separations than systems with larger values of ϵ_{wm} . This trend may also help explain differences in experiments, as variations in the effective value of ϵ_{wm} (e.g., related to the surface ion concentration in the cleaved mica) may shift the confinement-induced transition.

Furthermore, it is important to note that typical simulations are performed with surface contact areas $\sim 10^{-5}$ to $10^{-4} \mu\text{m}^2$, whereas experiments with the surface force balance (where solid phases are observed) have contact areas of $\sim 10^2 \mu\text{m}^2$ and experiments with the surface force apparatus (where solid phases are not observed) have $\sim 10^4 \mu\text{m}^2$.⁵⁴ The many-orders-of-magnitude difference in contact area may also play a significant role, influencing the dynamics and the ability to form the lowest free energy state. To investigate this, we perform GCMC simulations for increasing surface contact area, focusing on ordering with the central most layer; our interest is in whether the final structures are the same as those seen in the smaller simulations and how the time to order in these large simulations varies with pore contact area. Specifically, we simulate two systems with 960 000 and 6 220 000 particles, each that can accommodate six ideal layers. If we assume that $\sigma_w = 3.5 \text{ \AA}$, roughly the diameter of the potassium atoms in mica,³¹ we find that these systems have surface contact areas of $0.0021 \mu\text{m}^2$ (960 000 particles) and $0.014 \mu\text{m}^2$ (6 220 000 particles). Simulations are performed by first disordering the system at $T^* = 4.0$ and then instantaneously quenching to $T^* = 1.1$; we monitor the in-plane 2D hexagonal OP within the central most layer (i.e., $l = 3$ in Fig. 5) as a function of time. $T^* = 1.1$ places us just within the ordered regime predicted from the smaller system sizes (see Table I). In Fig. 7, we plot the OP as a function of time for the two system

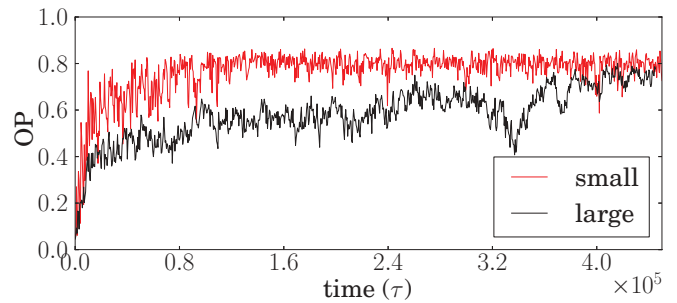


FIG. 7. (Color online) In-plane 2D hexagonal order parameter within the central most layers ($l = 3$) of a system that can accommodate six ideal layers as a function of time for *small* (960 000) particles and *large* (6 220 000) particles.

sizes. The larger system requires a significantly longer time, by a factor of ~ 5 , to reach the same level of ordering as the smaller system. The ratio of surface areas is ~ 6.6 ; extrapolating this trend, we would expect that a two-order-of-magnitude increase in surface contact area would result in the system requiring a factor of ~ 75 more time to reach an equivalently ordered state. Previous work⁵⁰ has focused on the connection between rate of compression of the surfaces (i.e., the time at each separation the system has to relax) and the structure, conjecturing that higher rates form nonequilibrium, jammed states. Clearly, this may be further exacerbated by surface-size effects, where systems with larger contact areas simply take much longer to reach equilibrium, and the significant effects that wall interaction strength and pore separation can have on the absolute free energy of the confined phase.

IV. CONCLUSION

In this work, we have combined GCMC simulations with absolute free energy measurements in studies of nanoconfined fluid phase behavior. We demonstrated that the free energy of nanoconfined system in the solid state decreases and the melting point for the nanoconfined fluid shifts to higher temperature as the wall-fluid interaction increases. We also showed that particles in contact with the pore walls demonstrate markedly different behavior than those in the central most region, where atoms in the central most region ultimately dictate the solidification. Using this, we calculated the Helmholtz free energy of the central region alone, factoring out the effects of the strong wall interactions. We found that the free energy of this central most region eventually converges to that of an equivalent density bulk liquid as the wall separation is increased; this convergence is a function of interaction strength, shifting to larger separations as wall-fluid strength increases. For systems with interaction strengths closely matching micaorganic molecule parameters, we find this transition occurs at roughly six layers, in good agreement with previous simulations and experiments. We also demonstrated the significant role that surface contact area plays in the ordering process; the additional time needed to order scales roughly with the ratio of surface contact area. These results provide additional evidence in support of the fluid-to-solid transition at ~ 6 molecule layers for nanoconfined nonpolar organic fluids.

It is important to note that our simulations and free energy calculations only explore the behavior of fluid/wall systems with commensurate fluid and wall molecular sizes. This is by design to simplify the analysis and enable comparison with bulk crystalline structures. Incommensurability of sizes may play an important role, shifting the free energy due to a competition between ordering dictated by the wall roughness and the preferred crystallinity and spacing of the fluid. Specifically, it has been observed that the relative orientation of herringbone structures observed for nanoconfined alkanes depends strongly on the structure of the walls;^{3,30,55} however, the accumulation of simulation results to date suggests that incommensurability does not lead to the elimination of the ODT. Nevertheless, comprehensively exploring the free energy landscape as a function of the ratio of wall-to-fluid particle size is of considerable interest and will be considered in future work.

ACKNOWLEDGMENTS

We gratefully acknowledge financial support from the National Science Foundation by Grant No. NSF CHE-0626259. T. D. Nguyen acknowledges the support from the Office of Science of the US Department of Energy under Contract No. DE-AC05-00OR22725. Computing resources are provided by National Energy Research Scientific Computing Center (supported by the Office of Science of the US Department of Energy under Contract No. DE-AC02-05CH11231), Oak Ridge Leadership Computing Facility at the Oak Ridge National Laboratory (supported by the Office of Science of the US Department of Energy under Contract No. DE-AC05-00OR22725), and the National Institute for Computational Sciences, Project-ID UT-TNEDU014 making use of the Keeneland cluster.⁵⁶

¹J. F. Xu, J. D. Kiely, Y. T. Hsia, and F. E. Talke, *Microsyst. Technol.: Micro. Nanosyst.-Inf. Stor. Process. Syst.* **15**, 687 (2009).
²M. Chen, W. H. Briscoe, S. P. Armes, and J. Klein, *Science* **323**, 1698 (2009).
³P. T. Cummings, H. Docherty, C. R. Iacovella, and J. K. Singh, *AIChE J.* **56**, 842 (2010).
⁴M. L. Gee, P. M. McGuiggan, J. N. Israelachvili, and A. M. Homola, *J. Chem. Phys.* **93**, 1895 (1990).
⁵J. Klein and E. Kumacheva, *Science* **269**, 816 (1995).
⁶J. Klein and E. Kumacheva, *J. Chem. Phys.* **108**, 6996 (1998).
⁷E. Kumacheva and J. Klein, *J. Chem. Phys.* **108**, 7010 (1998).
⁸A. L. Demirel and S. Granick, *Phys. Rev. Lett.* **77**, 2261 (1996).
⁹S. Granick, *Science* **253**, 1374 (1991).
¹⁰S. Ohnishi, M. Hato, K. Tamada, and H. K. Christenson, *Langmuir* **15**, 3312 (1999).
¹¹M. M. Kohonen, F. C. Meldrum, and H. K. Christenson, *Langmuir* **19**, 975 (2003).
¹²Y. Zhu and S. Granick, *Langmuir* **19**, 8148 (2003).
¹³M. Sliwinska-Bartkowiak, G. Dudziak, R. Sikorski, R. Gras, K. E. Gubbins, R. Radhakrishnan, and K. Kaneko, *Polish J. Chem.* **75**, 547 (2001).
¹⁴J. Czwartos, B. Coasne, K. E. Gubbins, F. R. Hung, and M. Sliwinska-Bartkowiak, *Mol. Phys.* **103**, 3103 (2005).
¹⁵S. Ohnishi, D. Kaneko, J. P. Gong, Y. Osada, A. M. Stewart, and V. V. Yaminsky, *Langmuir* **23**, 7032 (2007).
¹⁶T. Becker and F. Mugele, *Phys. Rev. Lett.* **91**, 166104 (2003).
¹⁷L. Bureau, *Phys. Rev. Lett.* **104**, 218302 (2010).
¹⁸A. Maali, T. Cohen-Bouhacina, G. Couturier, and J.-P. Aimé, *Phys. Rev. Lett.* **96**, 086105 (2006).
¹⁹G. B. Kaggwa, J. I. Kilpatrick, J. E. Sader, and S. P. Jarvis, *Appl. Phys. Lett.* **93**, 011909 (2008).
²⁰S. de Beer, D. van den Ende, and F. Mugele, *Nanotechnology* **21**, 325703 (2010).
²¹S. de Beer, W. K. den Otter, D. van den Ende, W. J. Briels, and F. Mugele, *Europhys. Lett.* **97**, 46001 (2012).
²²J. Israelachvili, Y. Min, M. Akbulut, A. Alig, G. Carver, W. Greene, K. Kristiansen, E. Meyer, N. Pesika, K. Rosenberg, and H. Zeng, *Rep. Prog. Phys.* **73**, 036601 (2010).
²³P. A. Thompson and M. O. Robbins, *Science* **250**, 792 (1990).
²⁴J. P. Gao, W. D. Luedtke, and U. Landman, *Phys. Rev. Lett.* **79**, 705 (1997).
²⁵S. T. Cui, P. T. Cummings, and H. D. Cochran, *J. Chem. Phys.* **111**, 1273 (1999).
²⁶L. D. Gelb, K. E. Gubbins, R. Radhakrishnan, and M. Sliwinska-Bartkowiak, *Rep. Prog. Phys.* **62**, 1573 (1999).
²⁷R. Radhakrishnan, K. E. Gubbins, and M. Sliwinska-Bartkowiak, *J. Chem. Phys.* **112**, 11048 (2000).
²⁸A. Jabbarzadeh, P. Harrowell, and R. I. Tanner, *Macromolecules (Washington, DC)* **36**, 5020 (2003).
²⁹A. Jabbarzadeh, P. Harrowell, and R. I. Tanner, *Phys. Rev. Lett.* **94**, 126103 (2005).
³⁰H. Docherty and P. T. Cummings, *Soft Matter* **6**, 1640 (2010).
³¹S. T. Cui, P. T. Cummings, and H. D. Cochran, *J. Chem. Phys.* **114**, 7189 (2001).
³²Y. S. Leng and P. T. Cummings, *Phys. Rev. Lett.* **94**, 026101 (2005).
³³Y. S. Leng and P. T. Cummings, *J. Chem. Phys.* **124**, 074711 (2006).
³⁴U. Raviv, S. Giasson, J. Frey, and J. Klein, *J. Phys.: Condens. Matter* **14**, 9275 (2002).
³⁵U. Raviv and J. Klein, *Science* **297**, 1540 (2002).
³⁶J. P. Gao, W. D. Luedtke, and U. Landman, *Phys. Rev. Lett.* **79**, 705 (1997).
³⁷D. Frenkel and A. J. C. Ladd, *J. Chem. Phys.* **81**, 3188 (1984).
³⁸J. M. Polson, E. Trizac, S. Pronk, and D. Frenkel, *J. Chem. Phys.* **112**, 5339 (2000).
³⁹J. A. Anderson, C. D. Lorenz, and A. Travasset, *J. Comput. Phys.* **227**, 5342 (2008).
⁴⁰<http://codeblue.umich.edu/hoomd-blue>.
⁴¹S. Plimpton, *J. Comput. Phys.* **117**, 1 (1995).
⁴²C. Vega and E. G. Noya, *J. Chem. Phys.* **127**, 154113 (2007).
⁴³C. Vega, E. Sanz, J. L. F. Abascal, and E. G. Noya, *J. Phys.: Condens. Matter* **20**, 153101 (2008).
⁴⁴See Supplemental Material at <http://link.aps.org/supplemental/10.1103/PhysRevB.86.214105> for a detailed derivation and validation of the modified tail correction.
⁴⁵H. Dominguez, M. P. Allen, and R. Evans, *Mol. Phys.* **96**, 209 (1999).
⁴⁶A. S. Keys, C. R. Iacovella, and S. C. Glotzer, *Annu. Rev. Condens. Matter Phys.* **2**, 263 (2011).

- ⁴⁷A. S. Keys, C. R. Iacovella, and S. C. Glotzer, *J. Comput. Phys.* **230**, 6438 (2011).
- ⁴⁸T. Kaneko, T. Mima, and K. Yasuoka, *Chem. Phys. Lett.* **490**, 165 (2010).
- ⁴⁹M. A. van der Hoef, *J. Chem. Phys.* **113**, 8142 (2000).
- ⁵⁰L. Bureau, *Phys. Rev. Lett.* **99**, 225503 (2007).
- ⁵¹J. Johnson, J. Zollweg, and K. Gubbins, *Mol. Phys.* **78**, 591 (1993).
- ⁵²J. Mittal, T. M. Truskett, J. R. Errington, and G. Hummer, *Phys. Rev. Lett.* **100**, 145901 (2008).
- ⁵³Y. Wu, G. Cheng, K. Katsov, S. W. Sides, J. Wang, J. Tang, G. H. Fredrickson, M. Moskovits, and G. D. Stucky, *Nat. Mater.* **3**, 816 (2004).
- ⁵⁴J. VanAlsten and S. Granick, *Phys. Rev. Lett.* **61**, 2570 (1988).
- ⁵⁵S. T. Cui, P. T. Cummings, and H. D. Cochran, *J. Chem. Phys.* **114**, 7189 (2001).
- ⁵⁶J. Vetter, R. Glassbrook, J. Dongarra, K. Schwan, B. Loftis, S. McNally, J. Meredith, J. Rogers, P. Roth, K. Spafford, and S. Yalamanchili, *Comput. Sci. Eng.* **13**, 90 (2011).